Tailoring polymer electrolyte solvation for 600 Wh kg^{-1} lithium batteries

https://doi.org/10.1038/s41586-025-09565-z

Received: 5 November 2024

Accepted: 21 August 2025

Published online: 24 September 2025

Check for updates

Xue-Yan Huang[1], Chen-Zi Zhao[1]✉, Wei-Jin Kong[1], Nan Yao[1], Zong-Yao Shuang[1], Pan Xu[1], Shuo Sun[1,2], Yang Lu[1,3], Wen-Ze Huang[1], Jin-Liang Li[1], Liang Shen[1], Xiang Chen[1], Jia-Qi Huang[4,5], Lynden A. Archer[6] & Qiang Zhang[1,7,8,9]✉

Polymer electrolytes paired with lithium-rich manganese-based layered oxide (LRMO) cathodes and anode-free cell design are considered one of the most promising high-energy-density and high-safety systems[1–4]. However, the unstable anode morphological changes and the irreversible anionic reactions at the electrolyte–cathode interfaces induce oxygen escape and catalytic decomposition of polymer electrolytes, resulting in severe interfacial degradation and poor cycling stability. Here we design an in-built fluoropolyether-based polymer electrolyte composed of strongly solvating polyether and weakly solvating fluorohydrocarbon pendants, creating an anion-rich solvation structure and thus anion-derived fluorine-rich interfacial layers on the cathode and anode to resist interfacial issues. The LRMO cathode exhibits improved oxygen redox reversibility with substantially reduced oxygen-involving interfacial side reactions. This quasi-solid-state polymer electrolyte with 30 wt% trimethyl phosphate enables an LRMO cathode with a reversible high-areal-capacity cycling (>8 mAh cm^{-2}) in pouch cells and long-term stability (>500 cycles at 25 °C) in coin cells, respectively. The pouch cells exhibit an energy density of 604 Wh kg^{-1} (1,027 Wh l^{-1}) and excellent safety under a nail penetration at a fully charged condition. Our work, therefore, provides a promising direction for creating practical high-energy-density and high-safety lithium batteries.

Solid-state batteries (SSBs) represent an important development in energy storage technology, offering superior energy density and safety compared with conventional lithium (Li)-ion batteries[5–10]. The use of high-capacity (more than 250 mAh g^{-1}) Li-rich manganese (Mn)-based layered oxide (LRMO)[11–13] cathodes, anode-free cell design and polymer electrolytes further boosts overall battery energy density[14,15] to more than 600 Wh kg^{-1}. Integrating LRMO and a copper (Cu) current collector with solid-state electrolytes (SSEs) can suppress transition metal ion dissolution, minimize parasitic reactions and enhance interfacial stability[16–18]. The LRMO cathodes achieve high specific capacities through dual redox reactions of both cationic ions and anionic ions above 4.5 V, but face challenges such as irreversible anionic redox and complex interfacial degradation at high voltages, especially when coupled with conventional polyether (PE)-based polymer electrolytes (Fig. 1a), which hinder Li$^+$ transfer kinetics[17]. Resolving the LRMO|SSE interfacial instability problem is important for practical SSBs.

In this study, we propose an anion solvation structure construction strategy to prepare an in-built fluoropolyether-based quasi-solid-state polymer electrolyte (FPE-SPE), which can improve the LRMO|SPE interfacial stability and accelerate interfacial kinetics in lithium batteries. The FPE-SPE with anion-rich solvation structure is formed by in situ polymerization of two miscible monomers: a strongly solvating polyether monomer and a weakly solvating fluorohydrocarbon monomer. The elaborately designed FPE-SPE potentially facilitates the dissociation of Li$^+$ from polymer chains and promotes anions to participate in contact ion pairs (CIPs) and aggregates (AGGs), which can finally form an inorganic fluorine-rich (F-rich) cathode electrolyte interphase (CEI) and solid electrolyte interphase (SEI) on the surface of LRMO and the anode, respectively. This CEI configuration generates an LiF outer layer with high-ionic-conductivity pathway to facilitate the activation of oxygen redox reactions, and an inner layer with Mn–F bonds to mitigate oxygen overoxidation on the LRMO surface (Fig. 1b). As a result, an anode-free pouch cell with FPE-SPE achieves an energy density of 604 Wh kg^{-1} and 1,027 Wh l^{-1}.

Structure and properties of FPE-SPE

The pioneering in-built polymer electrolytes offer a promising direction to construct conformal interfaces inside an electrochemical cell[19–22]. Specifically, poly(ethylene glycol) methyl ether acrylate (PE monomer) and fluorohydrocarbon monomer, such

---

[1]Beijing Key Laboratory of Complex Solid-State Batteries, Department of Chemical Engineering, Tsinghua University, Beijing, China. [2]School of Materials Science and Engineering, Nanjing Tech University, Nanjing, China. [3]National Energy Metal Resources and New Materials Key Laboratory, School of Metallurgy and Environment, Central South University, Changsha, China. [4]School of Interdisciplinary Science, Beijing Institute of Technology, Beijing, China. [5]School of Materials Science and Engineering, Beijing Institute of Technology, Beijing, China. [6]Robert Frederick Smith School of Chemical and Biomolecular Engineering, Cornell University, Ithaca, NY, USA. [7]State Key Laboratory of Chemical Engineering and Low-Carbon Technology, Tsinghua University, Beijing, China. [8]The Innovation Center for Smart Solid-State Batteries, Yibin, China. [9]Institute for Carbon Neutrality, Tsinghua University, Beijing, China. ✉e-mail: zcz@mail.tsinghua.edu.cn; zhang-qiang@mails.tsinghua.edu.cn

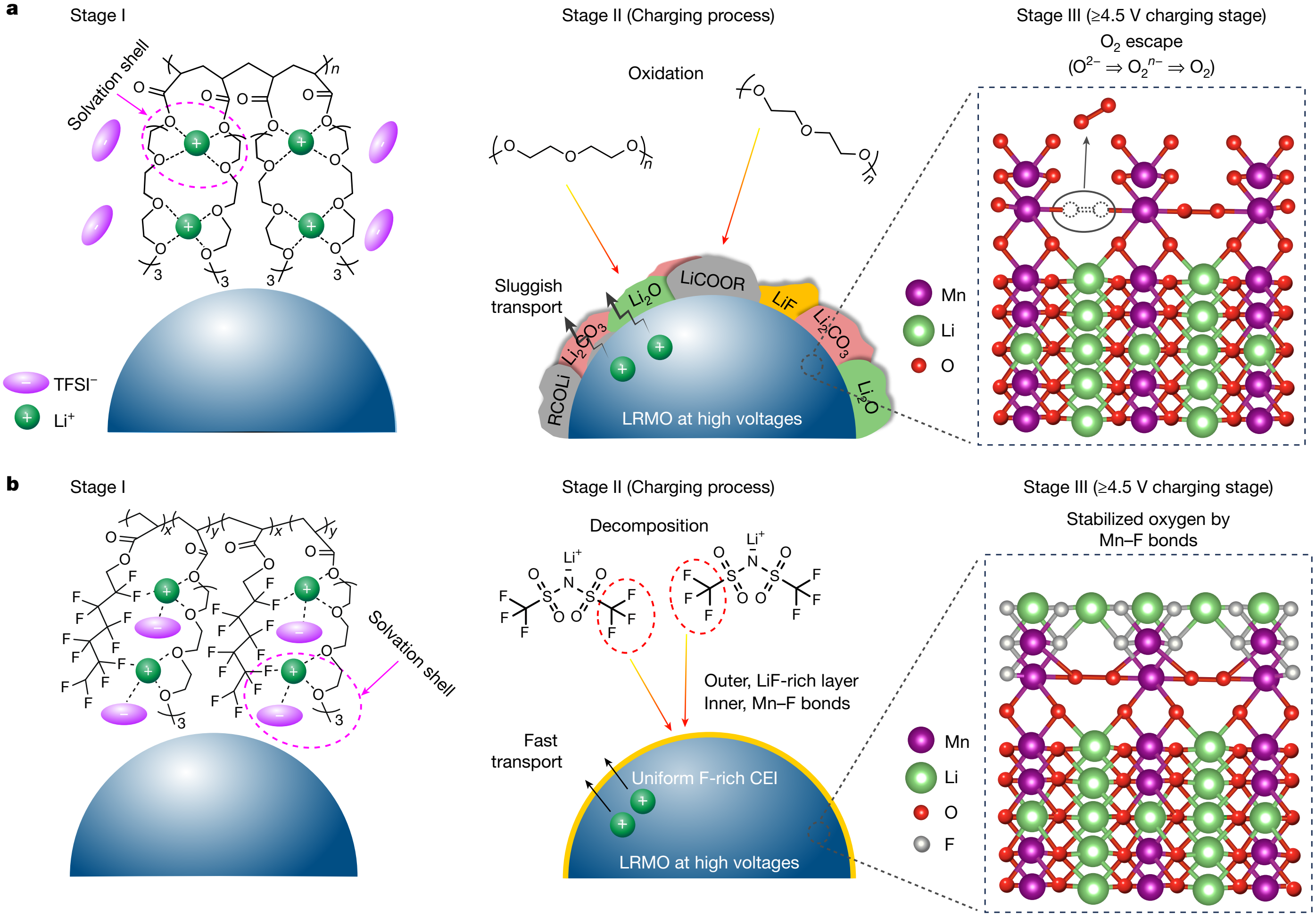

Fig. 1 | Schematic of designing fluoropolyether-based polymer electrolyte with anion-rich solvation structure. a, The polyether-based polymer electrolyte with overgrown CEI at the interface and surface oxygen instability of the LRMO cathode. The strong coordination between Li⁺ and ether oxygen generates anion-deficient solvation structure, whereas the poor oxidation stability of PE polymer electrolytes further causes interfacial decomposition. Stage I represents the in situ polyether-based electrolyte with anion-deficient solvation; stage II represents PE polymer oxidation at the charging process; and stage III represents the surface oxygen oxidized in LRMO, resulting in O_2 gas escape. **b**, Stabilized LRMO surface oxygen by anion-derived CEI in fluoropolyether-based polymer electrolyte. Stage I is the in situ fluoropolyether-based electrolyte with anion-rich solvation; stage II is anion decomposition at the charging process; and stage III is Mn–F bonds suppressing O_2 escape.

as 2,2,3,3,4,4,4-heptafluorobutyl acrylate (SF), 1H,1H,2H,2H-nonafluorohexyl acrylate (NF), 2,2,3,3,4,4,5,5,6,6,7,7-dodecafluoroheptyl acrylate (TF), were introduced and copolymerized in a molar ratio of 1:1 by thermally initiated radical polymerization to obtain copolymers (Fig. 2a), composite materials by adding lithium bis(trifluoromethanesulfonyl)imide (LiTFSI) and SPEs by adding LiTFSI and 30 wt% trimethyl phosphate (TMP) plasticizer, respectively. The chemical structures of as-synthesized polymers are confirmed in Supplementary Figs. 1–3.

Differential scanning calorimetry (DSC) analysis shows that typical peaks associated with the T_c and T_m are observed in the PE polymer, whereas T_c disappears and T_m decreases in fluoropolyether copolymer analogs as the fluorine atom number increases (Fig. 2b). It is evident that whereas the PE polymer is crystalline, PTF-PE copolymer is essentially amorphous. Low glass transition temperatures (T_g for copolymers = −62 °C to −56 °C, T_g for copolymers with LiTFSI = −49 °C to −45 °C) and high temperature tolerance (328 °C with 5% weight loss for copolymers with LiTFSI) are also found for fluoropolyether copolymers (Fig. 2b and Supplementary Figs. 4 and 5). Moreover, a low T_g of −75 °C is found for PTF-PE-SPE, contributing to effective Li⁺ transportation. PTF-PE/LiTFSI film exhibited flame-retardant property, achieving self-extinction on flame removal (Fig. 2c). After adding TMP plasticizer, the PTF-PE-SPE film stayed nonflammable before and after the fire removal, attributing to the inherently noncombustible nature of TMP (Supplementary Fig. 6). The rheological and mechanical properties of SPE were further studied; the PTF-PE-SPE exhibited elastic solid behaviour at 25 °C, and the stretching strain was 860% (Supplementary Figs. 7 and 8).

High oxidation stability of the SPEs is essential for LRMO-based batteries to achieve a high energy density. Electrochemical floating experiment shows superior oxidative stability of PTF-PE/LiTFSI at 5.0 V compared with PE/LiTFSI (3.6 V) (Fig. 2d and Supplementary Figs. 9 and 10). Density functional theory (DFT) calculations attribute this enhancement to the lower HOMO energy level (−7.96 eV compared with −7.50 eV) (Fig. 2e, Supplementary Figs. 11–15 and Supplementary Note 1). Moreover, the pronounced interactions between Li ions and electron-donating groups suggest the formation of Li bonds, balancing ion dissociation and migration dynamics[23]. Fluorinated segment length appears to correlate with voltage limit, as the strong electron-withdrawing effect of F atoms helps reduce lone-pair electron density on ether oxygens, contributing to decreased oxidation propensity. Solid-state nuclear magnetic resonance (NMR) confirms decreased electron density of the H atoms in the ether segment of the PTF-PE-SPE by downfield shift (Supplementary Fig. 16).

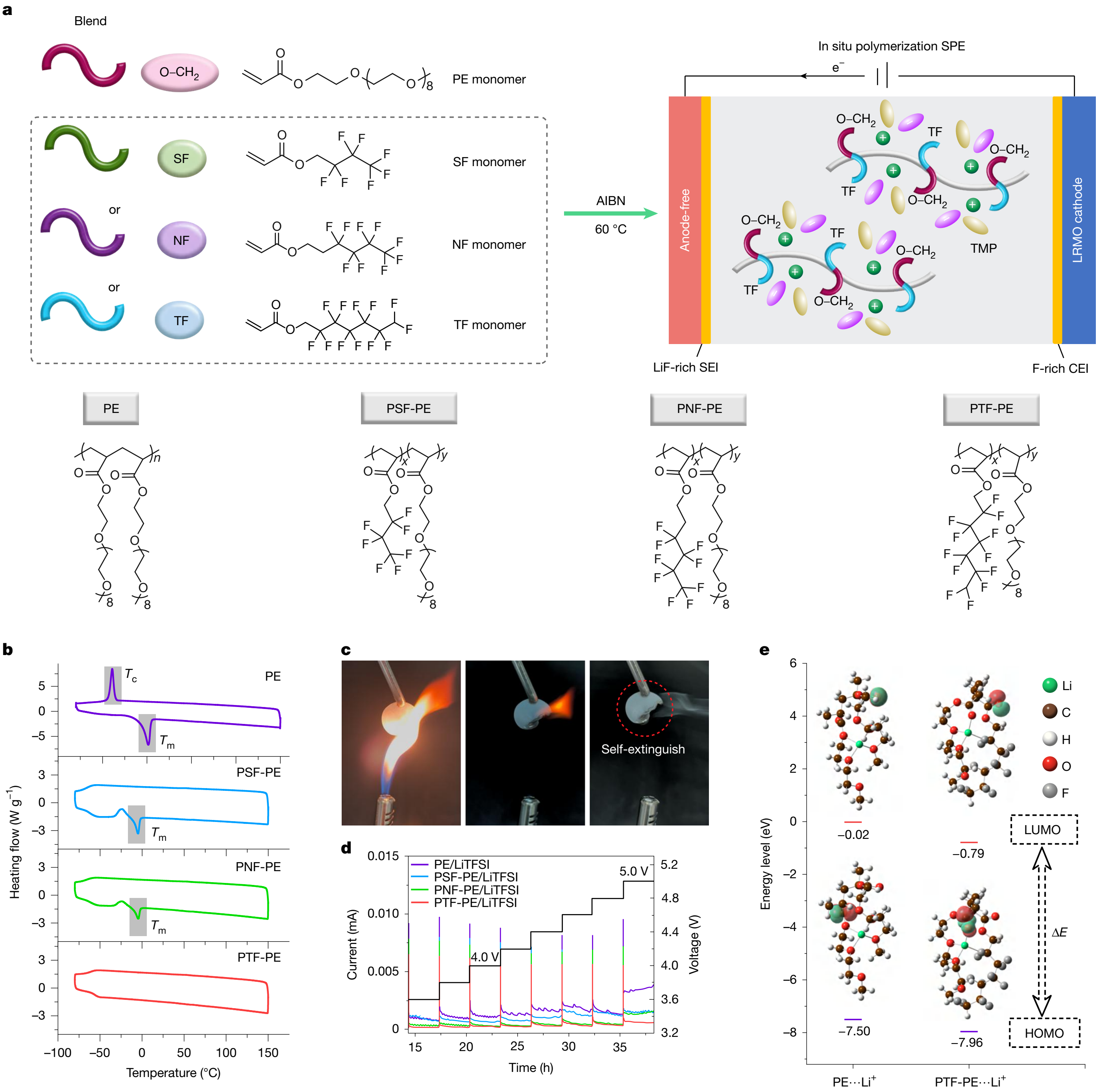

Fig. 2 | Design and fabrication of fluoropolyether-based SPEs. a, Schematic of synthesizing of fluoropolyether copolymers through in situ polymerization catalysed by 2,2′-azobis(2-methylpropionitrile) (AIBN). **b**, DSC analysis of PE and fluoropolyether copolymers. The shaded areas show the melting peak (T_m) and recrystallization peak (T_c). **c**, Specific burning test of PTF-PE/LiTFSI with separator. **d**, Electrochemical floating analysis of PE and fluoropolyether copolymers with LiTFSI. **e**, Highest occupied molecular orbital (HOMO) and lowest unoccupied molecular orbital (LUMO) energy levels of PE and PTF-PE coordinated with Li^+.

The F-based interactions were investigated by the 2D ^1H–^1H NOESY NMR spectrum. Although pristine PTF-PE copolymer shows no observable off-diagonal fluorohydrocarbon ^1H cross-peaks (Fig. 3a), the addition of LiTFSI induces distinct cross-peaks between fluorohydrocarbon protons ($-CH_2-CF_2-$/$-CHF_2$) and ether protons ($-O-CH_2-$) in polyether chains (Fig. 3b). The strong cross-relation indicates that the polyether chains and fluorohydrocarbon chains are closed by <10 Å (ref. 24), which can take place because of the $-F\cdots Li^+\cdots O-CH_2-$ intersegment interaction, enabling Li^+ transport between fluorohydrocarbon and polyether chains (Supplementary Fig. 17). ^1H and ^{19}F solid-state NMR experiments showed the interaction between Li^+ and $-CF_2$ fluorine atoms (Fig. 3c,d). The H atoms in the ether segment (3.2–4.2 ppm) shift to downfield (to lower electron density) owing to the effect of Li^+ on the lone-pair electron density of the oxygen in the ether group, whereas fluorohydrocarbon protons shift upfield because of the electron-withdrawing effect of F atoms on the Li^+. Meantime, the ^{19}F signals (117–130 ppm and 136–140 ppm) for $-CF_2$ shift upfield on Li^+ coordination. Moreover, the $-F\cdots Li^+$ interaction facilitates continuous Li^+ transmission pathways. Raman spectra were obtained to evaluate the solvation structure of fluoropolyether/LiTFSI systems (Fig. 3e).

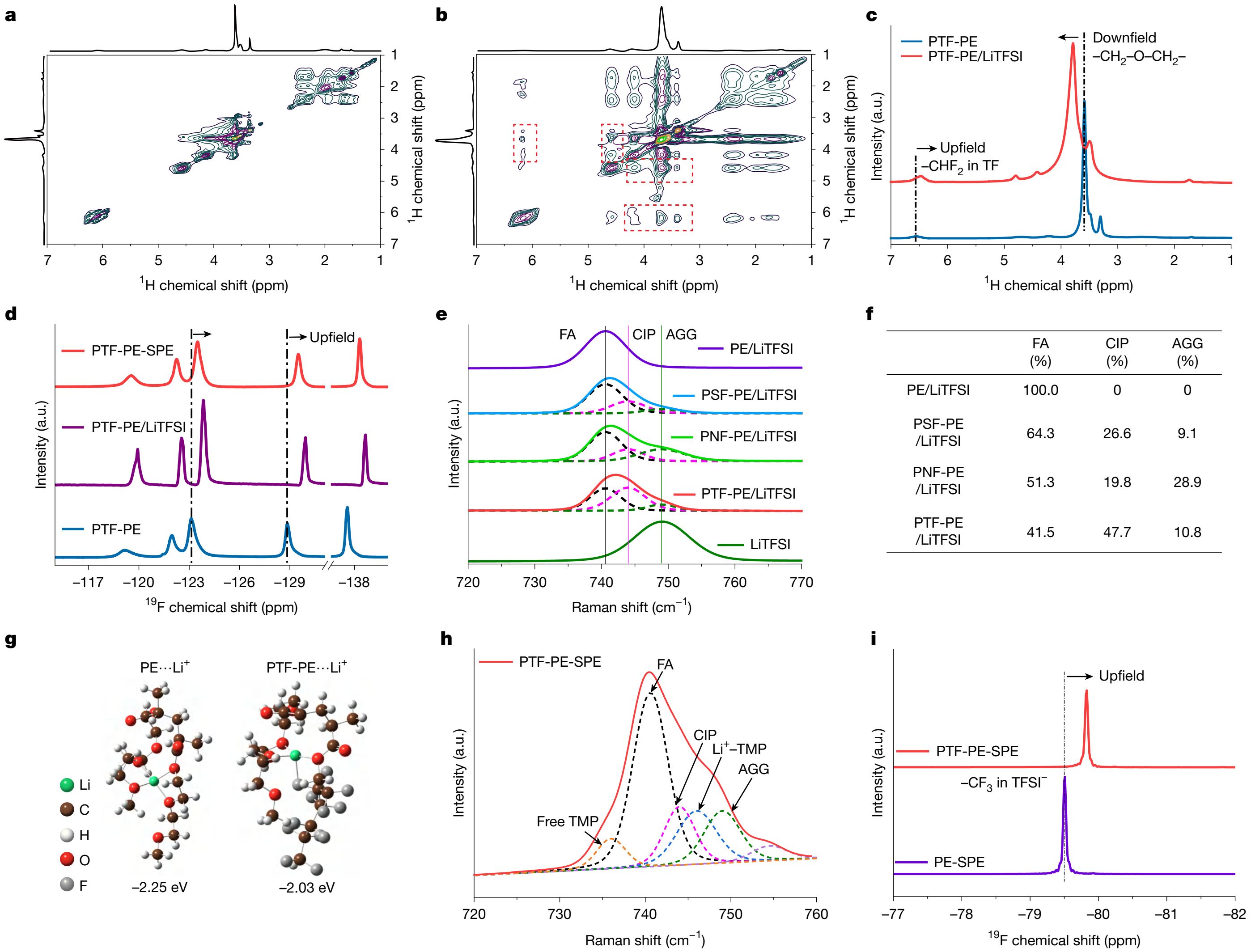

	FA (%)	CIP (%)	AGG (%)
PE/LiTFSI	100.0	0	0
PSF-PE /LiTFSI	64.3	26.6	9.1
PNF-PE /LiTFSI	51.3	19.8	28.9
PTF-PE /LiTFSI	41.5	47.7	10.8

Fig. 3 | Characterization of fluoropolyether-based SPEs. a,**b**, 2D ^{1}H–^{1}H NOESY NMR spectrum of PTF-PE (**a**) and PTF-PE/LiTFSI (**b**). The ^{1}H signals at 4.6 ppm (–CH$_2$–CF$_2$–) and 6.3 ppm (–CHF$_2$) are associated with the protons in fluorohydrocarbon chains, whereas ^{1}H signals at 3.4 ppm, 3.7 ppm and 4.2 ppm are associated with protons from the ether group in polyether chains. **c**, ^{1}H solid-state NMR of PTF-PE and PTF-PE/LiTFSI. **d**, Changes of chemical shift in ^{19}F solid-state NMR for PTF-PE, PTF-PE/LiTFSI and PTF-PE-SPE. **e**, S–N–S stretching of TFSI$^-$ in coordination with Li$^+$, indicating the formation of CIPs and AGGs. The solvation structure was evaluated by comparing the S–N–S symmetric stretching band (ν_s(SNS)) of TFSI$^-$. **f**, The amount of free anions (FA), CIPs and AGGs. The FA peak at 740.6 cm^{-1}, CIP peak at 744 cm^{-1} and AGG peak at 749 cm^{-1}. **g**, DFT calculation of Li$^+$ binding energy for PE and PTF-PE. **h**, Raman spectra of PTF-PE-SPE. **i**, Changes of chemical shift in ^{19}F solid-state NMR for PE-SPE and PTF-PE-SPE. a.u., arbitrary units.

Although LiTFSI shows mainly AGGs structure, blending with PE yields more free anions (740.6 cm^{-1}), indicating Li$^+$–ether oxygen coordination. In fluoropolyether copolymers, ν_s(SNS) shifts to 744–749 cm^{-1}, demonstrating CIPs/AGGs formation by –F···Li$^+$···O–CH$_2$– coordination (Supplementary Fig. 18 and Supplementary Note 2). Increasing fluorocarbon chain length raised the summation of AGGs and CIPs proportions from 35.7% (PSF-PE) to 58.5% (PTF-PE), with free anions proportion dropping to 41.5% (Fig. 3f), indicating enhanced TFSI$^-$ binding in solvation sheaths. DFT calculations showed the weaker binding energy between PTF-PE and Li$^+$ (−2.03 eV) than that between PE and Li$^+$ (−2.25 eV) (Fig. 3g and Supplementary Fig. 19), facilitating Li$^+$ transport with lower activation energy (Supplementary Fig. 20 and Supplementary Note 3). Notably, there are CIPs/AGGs solvation structures in PTF-PE-SPE, whereas predominantly free anions can be observed in PE-SPE (Fig. 3h and Supplementary Fig. 21). ^{19}F solid-state NMR signal shifts upfield to −79.8 ppm, suggesting the presence of special interactions in PTF-PE-SPE (Fig. 3i). PTF-PE-SPE exhibits a higher Li$^+$ transference number of 0.40 compared with PE-SPE (0.34) (Supplementary Fig. 22). These results suggest the potential role of fluorohydrocarbon chain in forming CIPs and AGGs solvation structures of PTF-PE-SPE.

Interfacial structural evolution and chemical mechanisms

To further explore the effect of the CIPs/AGGs solvation structure on facilitating an anion-rich-derived CEI/SEI, LRMO-based lithium metal batteries (LMBs) were assembled to investigate the electrochemical behaviour of SPEs. The initial Coulombic efficiency (CE) and specific discharge capacity are 91.8% and 290.3 mAh g^{-1} for LMB with PTF-PE-SPE, respectively, much higher than that of PE-SPE (74.8%, 270.5 mAh g^{-1}) because of the improved reversibility of oxygen redox in LRMO cathode (Supplementary Fig. 23). Supplementary Fig. 24 and Supplementary Note 4 show the internal impedance evolution of LMBs. As expected, the PTF-PE-SPE exhibits a small change in the internal impedance, proving the effective suppression of the decomposition of SPE. X-ray photoelectron spectroscopy (XPS) results indicated that the PTF-PE-SPE improved cathode interfacial stability during charging (Supplementary Figs. 25–27

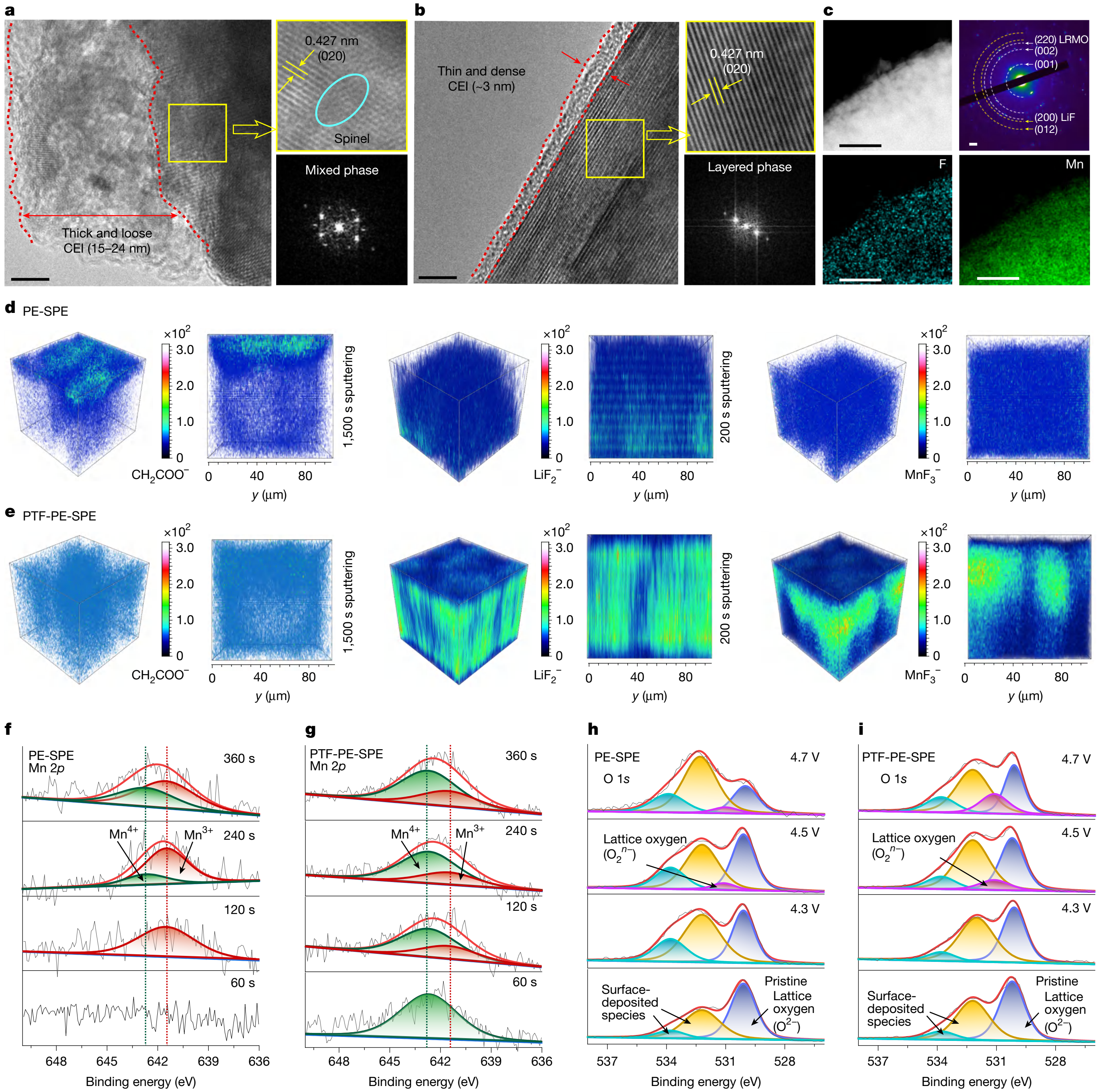

Fig. 4 | CEI composition of PE-SPE and PTF-PE-SPE with LRMO. a,**b**, TEM images of LRMO cathodes using PE-SPE (**a**) and PTF-PE-SPE (**b**) after 100 cycles and FFT of the selected areas highlighted in yellow. **c**, EDS mappings of F and Mn, and SAED image for the cycled LRMO cathode using PTF-PE-SPE. **d**,**e**, TOF-SIMS 3D and 2D tomography of the LRMO cathodes after 100 cycles using PE-SPE (**d**) and PTF-PE-SPE (**e**). **f**,**g**, Mn 2*p* XPS spectra of cycled LRMO cathodes with PE-SPE (**f**) and PTF-PE-SPE (**g**) under different sputtering depths. **h**,**i**, O 1*s* XPS spectra after 120 s sputtering depth of LRMO cathodes using PE-SPE (**h**) and PTF-PE-SPE (**i**) during the initial charging process. Scale bars, 5 nm (**a**,**b**); 500 nm (**c**).

and Supplementary Notes 5 and 6). The compatibility of PTF-PE-SPE with Li metal anode is evaluated, which is comparably essential for the performance of lithium batteries (Supplementary Figs. 28–33 and Supplementary Notes 7–9). As demonstrated, PTF-PE-SPE has induced the formation of anion-derived LiF-rich SEI, resulting in highly reversible Li plating/stripping.

The interfacial structural evolution has been evaluated to seek a better understanding of the underlying interfacial chemistries. A transmission electron microscopy (TEM) image shows a thick and loose CEI (15–24 nm) on the LRMO cathode with PE-SPE. By contrast, a dense and thin LiF-rich CEI (3 nm) is seen uniformly covering the LRMO cathode when PTF-PE-SPE (Fig. 4a,b) is used, contributing to the lower polarization and resistance. Fast Fourier transform (FFT) and selected area electron diffraction (SAED) analyses showed preserved lattice integrity of cycled LRMO in the PTF-PE-SPE, whereas the PE-SPE induced lattice fringe distortion and spinel-like phase formation because of oxygen escape (Fig. 4c and Supplementary Fig. 34). Lattice planes of LiF ((200) and (012)) were identified by SAED, whereas TEM-energy-dispersive spectroscopy (EDS) mapping suggested the uniform F and Mn distribution. This observation indicates that the

LiF-rich CEI can effectively suppress the irreversible phase transition of LRMO and stabilize its layered structure. Time-of-flight secondary ion mass spectrometry (TOF-SIMS) and XPS have been used to examine the chemical compositions of CEI layers and cathode surface for cycled LRMO (Fig. 4d,e and Supplementary Figs. 35 and 36). It can be observed that rich CH_2COO^- and CH_2CHO^- species predominate the surface layer of cycled LRMO with PE-SPE, whereas LiF_2^- species are sparse. Conversely, the cycled LRMO with PTF-PE-SPE exhibited an inverse compositional structure, with LiF_2^- tending to accumulate in the surface layer of the cathode. Furthermore, MnF_3^- species can be distinctly observed on the subsurface of the LRMO with PTF-PE-SPE, exhibiting a species distribution markedly different from that of LRMO with PE-SPE, suggesting that the F doping penetrates deep into the surface lattice of the LRMO cathode through the anion substitution (F atom exchanges with O atom), which further improves the surface structure stability of the LRMO because of the strong Mn–F bonds.

Here, XPS analysis and ex situ Raman spectra were used to investigate the effect of Mn–F bonds on the surface chemistry evolution of the LRMO cathode (Fig. 4f–i and Supplementary Fig. 37). Note that the Mn 2*p* signal is less likely to be generated from LRMO with PE-SPE under the same sputtering condition for 60 s depth because of the overgrown CEI. To maintain the neutrality of the cathode particles, it is suggested that Mn^{4+} goes through reduction to Mn^{3+} on oxygen loss[11]. Here, Mn from the surface of cycled LRMO with PE-SPE experiences reduction to Mn^{3+} (Fig. 4f), indicating ongoing oxygen escape at the same time[25,26]. This is also supported by the O 1*s* XPS and Raman spectra on the surface of LRMO cathodes. For the O 1*s* spectra in the PE-SPE (Fig. 4h), the two-peak characteristic of O^{2-} anions belonging to the lattice oxygen (530.0 eV peak) and weakly adsorbed surface species are observed[27]. The intensity variation of lattice O^{2-} during charging implies its link with O^{2-} anionic redox. The intensity of surface deposited species increases when the sample is charged to 4.3 V, and a new component at 531.1 eV for the 4.5 V charged sample appears, attributed to the existence of O_2^{n-} ($n \leq 2$) or to under-coordinated oxygen atoms. When charging to 4.7 V, the intensity of the O_2^{n-} peak barely changes, but the lattice O^{2-} decreases compared with that for 4.5 V. The reduction of lattice O^{2-} and the invariable intensity of O_2^{n-} suggests that the lattice oxygen undergoes a continuous $O^{2-} \Rightarrow O_2^{n-} \Rightarrow O_2$ oxidation and ultimately forms gaseous O_2 at high charging voltages (>4.5 V), resulting in an irreversible O oxidation process (Supplementary Figs. 38 and 39). The Mn 2*p* binding energy in LRMO exhibits a negative shift during the high charging state of >4.5 V, which is related to O overoxidation (Supplementary Fig. 40a).

Turning to LRMO with PTF-PE-SPE, the most obvious difference is the presence of the Mn^{4+} component on the surface of LRMO instead of Mn^{3+} after cycling, indicating that the strong Mn–F bonds at the LRMO surface contribute to stabilizing the valence state of Mn and suppressing O^{2-} irreversible oxidation (Fig. 4g). F anion substitution stabilizes lattice oxygen and enhances the reversibility of oxygen redox, inhibiting the oxygen escape. (Supplementary Fig. 38b). Moreover, the results indicate that more O_2^{n-} has generated and the slight reduction of lattice O^{2-} occurs simultaneously when charged to 4.7 V, suggesting the maximization of the stage $O^{2-} \Rightarrow O_2^{n-}$ without detectable oxygen escape (Fig. 4i and Supplementary Fig. 41). This observation is further supported by the Mn 2*p* spectra, which exhibit no significant change in Mn valence state (Supplementary Fig. 40b). In particular, the peroxide-related O_2^{2-} and superoxide-related O_2^- signal disappeared in Raman spectra, indicating that the O_2^{n-} species was trapped in the lattice. In brief, the findings from interfacial evolution can be summarized using three aspects: (1) PTF-PE-SPE possessing weakly solvating ability builds an anion-derived F-rich surface on the electrodes; (2) LiF-rich CEI/SEI can effectively suppress the phase transition of LRMO and Li metal anode pulverization; and (3) O atoms in the lattice of the subsurface of LRMO cathode are substituted by F atoms to build the stable Mn–F bond, which tunes oxygen redox, traps the oxidized lattice oxygen O_2^{n-} species and suppresses the O_2 release, ultimately delivering a higher specific capacity.

Electrochemical and safety performance of lithium batteries

Long-term cycling performance of Li|SPE|LRMO cells at 1.0 C is shown in Supplementary Fig. 42. The LMB with PTF-PE-SPE exhibits limited capacity decay, retaining 80.2% capacity after 200 cycles with an average CE of 99.7%, whereas PE-SPE suffers fast capacity decay with 80% capacity retention over only 50 cycles and a lower average CE of 98.7%. The discharge voltage decay of LMB using PTF-PE-SPE shows only about 1.54 mV per cycle compared with 2.69 mV per cycle for PE-SPE (Supplementary Fig. 43). The d*Q*/d*V* (differential capacity over voltage) curves similarly show the obvious suppression of the voltage decay in the PTF-PE-SPE compared with that in the PE-SPE (Supplementary Fig. 44). The charge and discharge curves of the LMBs with different SPEs from the 3rd to 200th cycle at 1.0 C was contrasted (Supplementary Fig. 45). The capacity contribution related to oxygen redox at voltage ranges over 3.75 V. In contrast to the obvious voltage decay of the Li|PE-SPE|LRMO, the curve of Li|PTF-PE-SPE|LRMO maintains a higher and more stable voltage. This severe voltage decay, especially the voltage plateau during the oxygen redox process, is attributed to the polarization effect caused by the overgrown CEI and the lattice oxygen escape, leading to capacity degradation.

The PTF-PE-SPE design demonstrates remarkable interfacial stability, enabling reversible oxygen redox in LRMO cathodes. The Li|PTF-PE-SPE|LRMO cell maintains 72.1% capacity retention with an average CE of 99.5% after 500 cycles at 0.5 C (Fig. 5a). Furthermore, the Li|PTF-PE-SPE|LRMO cell delivers a reversible capacity of 222.2 mAh g^{-1} and 191.3 mAh g^{-1} at 0.5 C and 1.0 C, respectively, demonstrating a superior rate ability (Fig. 5b and Supplementary Fig. 46). Galvanostatic intermittent titration technique (GITT) analysis shows that LRMO with PTF-PE-SPE shows better Li^+ ion transport kinetics than that with PE-SPE (Supplementary Fig. 47), which indicates the accelerated Li^+ insertion/extraction kinetics of LRMO, because of the reduction in surface charge transfer impedance by the contribution of stable CEI layer and the increase in ion mobility in the bulk phase. The advantage of PTF-PE-SPE also made it suitable for $LiNi_{0.8}Co_{0.1}Mn_{0.1}O_2$ cathode, achieving 90% capacity retention after 200 cycles (Supplementary Fig. 48).

Anode-free Cu|PTF-PE-SPE|LRMO pouch cells with no excess lithium and lean SPE (electrolyte to capacity ratio, *E/C* ratio, 1.2 g Ah^{-1}) were assembled and evaluated to demonstrate the effectiveness of PTF-PE-SPE (Fig. 5c,d, Supplementary Figs. 49–51 and Supplementary Table 1). Notably, the Cu|PTF-PE-SPE|LRMO pouch cell achieves a discharge capacity of 8.96 Ah and a high initial specific energy of 604 Wh kg^{-1}/1,027 Wh l^{-1} (0.05 C) based on the total weight and volume of the pouch cell and maintains a discharge capacity of 6.66 Ah after 15 cycles under 25 °C (Fig. 5e). The measured value of specific energy achieved in this work is much higher than the reported state-of-the-art Li metal pouch cells with polymer or inorganic electrolytes[28–33] (Fig. 5f), illustrating the extraordinary effectiveness of PTF-PE-SPE in practical lithium batteries.

The PTE-PE-SPE also provides high-safety performance for the high-energy LMBs. As shown in Supplementary Figs. 52 and 53, the fully charged (4.7 V, after cycling) Li|PTF-PE-SPE|LRMO pouch cell did not catch fire during a nail penetration process and a thermal test (storing at 120 °C for 6 h). Furthermore, extended volume-accelerating rate calorimeter (EV-ARC) analysis shows that the T_{onset} and T_{tr} of Li|PTF-PE-SPE|LRMO were 85.4 °C and 216.0 °C, respectively. By contrast, the T_{onset} and T_{tr} of the pouch cell with liquid electrolyte were 33.5 °C and 122.6 °C, respectively. Furthermore, the voltage was also well maintained above 3.6 V during the EV-ARC test, proving that the pouch cell with PTF-PE-SPE did not experience a serious internal short circuit before suffering from thermal runaway (Fig. 5g,h). We deduce that the charged LRMO cathode-released oxygen at a critical temperature, consumed by

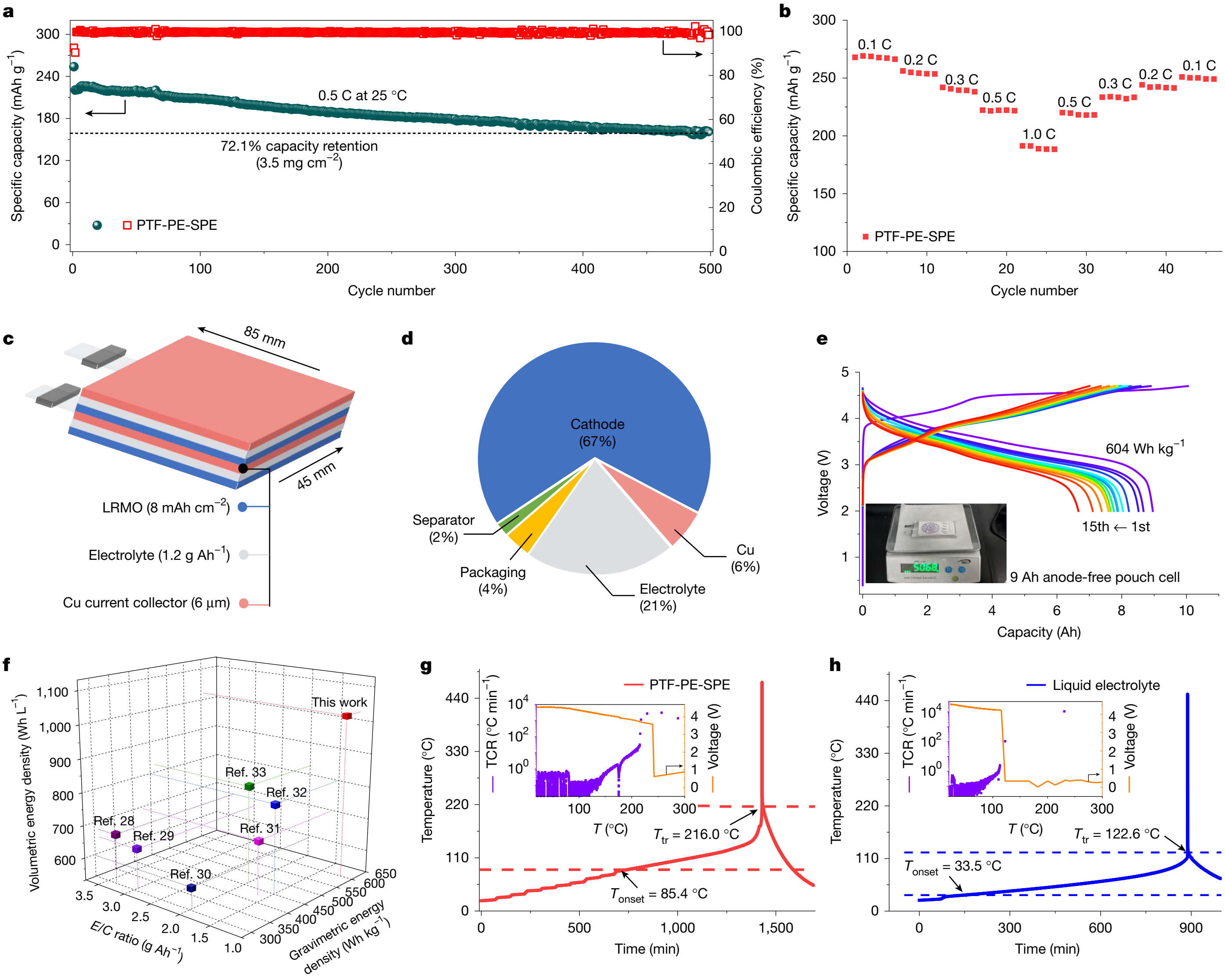

Fig. 5 | Electrochemical and safety performances of PTF-PE-SPE. a, The long-term cycling of LRMO-based LMB using PTF-PE-SPE at 0.5 C. **b**, Rate performance of LRMO-based LMB using PTF-PE-SPE at 25 °C. **c**, Schematic of an anode-free pouch cell (Cu|PTF-PE-SPE|LRMO) of 600 Wh kg^{-1}. **d**, Weight ratios of cell components (pink, Cu 6%; golden, packaging 4%; and green, separator 2%) in the reported pouch cell; detailed information is provided in Supplementary Table 1. **e**, The voltage profiles of a 9 Ah anode-free pouch cell from the 1st to the 15th cycles at 0.05 C. The inset shows an optical image taken during the weighting process for an energy density calculation. **f**, The performances of high-energy-density Li metal pouch cells in published literature and this work (criteria: energy density ≥300 Wh kg^{-1}). **g**,**h**, Thermal runaway features of fully charged Li|PTF-PE-SPE|LRMO pouch cell (**g**) and Li|liquid electrolyte|LRMO pouch cell (**h**) in EV-ARC tests. T_{onset} is the heat-releasing onset temperature and T_{tr} is the thermal runaway temperature. TCR, temperature change rate.

the Li metal anode, therefore, triggered the thermal runaway process. For the pouch cell with liquid electrolyte, the cell underwent thermal runaway when an internal short circuit occurred. Nevertheless, improving the T_{onset} and T_{tr} by PTF-PE-SPE can reduce potential damage when LRMO-based LMBs experience thermal runaway.

Conclusions

An in-built fluoropolyether-based PTF-PE-SPE was successfully synthesized by thermal-induced in situ polymerization. This polymer electrolyte creates anion-derived F-rich CEI/SEI, which stabilizes LRMO cathodes and enables the deposition of dense Li metal on the current collector. Specifically, the successful protection of the LRMO cathode by PTF-PE-SPE was ascribed to the suppression of surface oxygen escape, structural transition and electrolyte decomposition, benefiting from the formation of an F-rich layer, including Mn−F bond and LiF species covering on LRMO cathode. This approach markedly strengthens the interfacial stability of the LRMO cathode, thereby facilitating improved oxygen participation in redox reactions and delivering a higher specific capacity. Consequently, the assembled LRMO-based LMBs delivered a high initial CE of 91.8% at 0.05 C and stable charge/discharge reversibility (CE = 99.7%) at 1.0 C after more than 200 cycles at 25 °C. This work establishes a precedent for a strategy to synthesize in-built polymer electrolytes that form a stable interfacial layer, enabling the development of practical lithium batteries with enhanced energy density and safety.

Online content

Any methods, additional references, Nature Portfolio reporting summaries, source data, extended data, supplementary information, acknowledgements, peer review information; details of author contributions and competing interests; and statements of data and code availability are available at https://doi.org/10.1038/s41586-025-09565-z.

1. Luo, D. et al. A Li-rich layered oxide cathode with negligible voltage decay. *Nat. Energy* **8**, 1078–1087 (2023).
2. Wang, L., Liu, T., Wu, T. & Lu, J. Strain-retardant coherent perovskite phase stabilized Ni-rich cathode. *Nature* **611**, 61–67 (2022).
3. Lee, Y.-G. et al. High-energy long-cycling all-solid-state lithium metal batteries enabled by silver–carbon composite anodes. *Nat. Energy* **5**, 299–308 (2020).
4. Deysher, G. et al. Design principles for enabling an anode-free sodium all-solid-state battery. *Nat. Energy* **9**, 1161–1172 (2024).
5. Krauskopf, T., Richter, F. H., Zeier, W. G. & Janek, J. Physicochemical concepts of the lithium metal anode in solid-state batteries. *Chem. Rev.* **120**, 7745–7794 (2020).
6. Ning, Z. et al. Dendrite initiation and propagation in lithium metal solid-state batteries. *Nature* **618**, 287–293 (2023).
7. Wan, H., Wang, Z., Zhang, W., He, X. & Wang, C. Interface design for all-solid-state lithium batteries. *Nature* **623**, 739–744 (2023).
8. Tarascon, J.-M. & Armand, M. Issues and challenges facing rechargeable lithium batteries. *Nature* **414**, 359–367 (2001).
9. Winter, M., Barnett, B. & Xu, K. Before Li ion batteries. *Chem. Rev.* **118**, 11433–11456 (2018).
10. Zhang, Q.-K. et al. Homogeneous and mechanically stable solid–electrolyte interphase enabled by trioxane-modulated electrolytes for lithium metal batteries. *Nat. Energy* **8**, 725–735 (2023).
11. Enyuan, H. et al. Evolution of redox couples in Li- and Mn-rich cathode materials and mitigation of voltage fade by reducing oxygen release. *Nat. Energy* **3**, 690–698 (2018).
12. Seo, D.-H. et al. The structural and chemical origin of the oxygen redox activity in layered and cation-disordered Li-excess cathode materials. *Nat. Chem.* **8**, 692–697 (2016).
13. Sharpe, R. et al. Redox chemistry and the role of trapped molecular O_2 in Li-rich disordered rocksalt oxyfluoride cathodes. *J. Am. Chem. Soc.* **142**, 21799–21809 (2020).
14. Albertus, P. et al. Challenges for and pathways toward Li-metal-based all-solid-state batteries. *ACS Energy Lett.* **6**, 1399–1404 (2021).
15. Li, Q., Yang, Y., Yu, X. & Li, H. A 700 $W \cdot h \cdot kg^{-1}$ rechargeable pouch type lithium battery. *Chinese Phys. Lett.* **40**, 048201 (2023).
16. Chen, B. et al. Achieving the high capacity and high stability of Li-rich oxide cathode in garnet-based solid-state battery. *Angew. Chem. Int. Ed.* **63**, e202315856 (2024).
17. Kong, W.-J. et al. From liquid to solid-state batteries: Li-rich Mn-based layered oxides as emerging cathodes with high energy density. *Adv. Mater.* **36**, 2310738 (2024).
18. Sun, S. et al. Eliminating interfacial O-involving degradation in Li-rich Mn-based cathodes for all-solid-state lithium batteries. *Sci. Adv.* **8**, eadd5189 (2022).
19. Zhao, Q., Liu, X., Stalin, S., Khan, K. & Archer, L. A. Solid-state polymer electrolytes with in-built fast interfacial transport for secondary lithium batteries. *Nat. Energy* **4**, 365–373 (2019).
20. Liu, Y. et al. In situ polymerization of 1,3-dioxane as a highly compatible polymer electrolyte to enable the stable operation of 4.5 V Li-metal batteries. *Energy Environ. Sci.* **16**, 6110–6119 (2023).
21. Zhu, J. et al. Long-cycling and high-voltage solid state lithium metal batteries enabled by fluorinated and crosslinked polyether electrolytes. *Angew. Chem. Int. Ed.* **63**, e202400303 (2024).
22. Yu, J. et al. In situ fabricated quasi-solid polymer electrolyte for high-energy-density lithium metal battery capable of subzero operation. *Adv. Energy Mater.* **12**, 2102932 (2022).
23. Yao, N. et al. Identifying the lithium bond and lithium ionic bond in electrolytes. *Chem* **11**, 102254 (2025).
24. Guo, D. et al. Foldable solid-state batteries enabled by electrolyte mediation in covalent organic frameworks. *Adv. Mater.* **34**, 2201410 (2022).
25. Liu, T. et al. Origin of structural degradation in Li-rich layered oxide cathode. *Nature* **606**, 305–312 (2022).
26. Zhang, H., Liu, H., Piper, L. F. J., Whittingham, M. S. & Zhou, G. Oxygen loss in layered oxide cathodes for Li-ion batteries: mechanisms, effects, and mitigation. *Chem. Rev.* **122**, 5641–5681 (2022).
27. Peng, J. et al. Phase compatible $NiFe_2O_4$ coating tunes oxygen redox in Li-rich layered oxide. *ACS Nano* **15**, 11607–11618 (2021).
28. Fan, W. et al. “Peapod-like” fiber network: a universal strategy for composite solid electrolytes to inhibit lithium dendrite growth in solid-state lithium metal batteries. *Nano Lett.* **24**, 9050–9057 (2024).
29. Lee, W. et al. Advanced parametrization for the production of high-energy solid-state lithium pouch cells containing polymer electrolytes. *Nat. Commun.* **15**, 5860 (2024).
30. Hu, J. K. et al. High energy density solid-state lithium metal batteries enabled by in situ polymerized integrated ultrathin solid electrolyte/cathode. *Adv. Funct. Mater.* **34**, 2311633 (2024).
31. Wang, H. et al. A strongly complexed solid polymer electrolyte enables a stable solid state high-voltage lithium metal battery. *Energy Environ. Sci.* **15**, 5149–5158 (2022).
32. Guo, J.-C. et al. A self-reconfigured, dual-layered artificial interphase toward high-current-density quasi-solid-state lithium metal batteries. *Adv. Mater.* **35**, 2300350 (2023).
33. Xu, P. et al. Solvation regulation reinforces anion-derived inorganic-rich interphase for high-performance quasi-solid-state Li metal batteries. *Adv. Mater.* **36**, 2409489 (2024).

Publisher’s note Springer Nature remains neutral with regard to jurisdictional claims in published maps and institutional affiliations.

Springer Nature or its licensor (e.g. a society or other partner) holds exclusive rights to this article under a publishing agreement with the author(s) or other rightsholder(s); author self-archiving of the accepted manuscript version of this article is solely governed by the terms of such publishing agreement and applicable law.

© The Author(s), under exclusive licence to Springer Nature Limited 2025

Methods

Materials and polymer electrolytes

SF (97% purity), NF (97% purity), TF (97% purity), poly(ethylene glycol) methyl ether acrylate (PE monomer, average $M_n = 480\ \mathrm{g\ mol^{-1}}$) and AIBN (99% purity) were purchased from Sigma-Aldrich. LiTFSI (99.9% purity) and TMP (99.9% purity) were purchased from Suzhou Duoduo Chemical Technology. Li foils (50 µm in thickness) were purchased from China Energy Lithium. Polyethylene separator was purchased from Asahi Kasei Technosystem. The $Li_{1.2}Mn_{0.54}Co_{0.13}Ni_{0.13}O_2$ (LRMO)[34] cathode with 8.0 mAh $\mathrm{cm^{-2}}$ for a pouch cell was prepared by mixing 97 wt% LRMO, 1.5 wt% polyvinylidene fluoride binder, 1 wt% Super and 0.5 wt% carbon fibre. For the low loading (about 3–4 mg $\mathrm{cm^{-2}}$) cathode, the cathode slurry was fabricated by mixing 80 wt% LRMO, 10 wt% Super P and 10 wt% PVDF (Alfa Aesar) in *N*-methyl-2-pyrrolidone (NMP, Aldrich) solution. The cathodes were obtained by coating the slurry onto aluminium (Al) foil using a knife coater and dried in a vacuum oven at 80 °C for over 12 h. A mixed precursor solution of fluorohydrocarbon monomer (SF, NF and TF) and PE monomer in a molar ratio of 1:1, with 0.2 wt% AIBN was stirred for 4 h at 25 °C and then heated at 60 °C to initiate the polymerization for 4 h. The quasi-solid-state polymer electrolytes were synthesized by thermal initiation of in situ polymerization. LiTFSI (24 wt%) was dissolved in a mixed solution of TF and PE monomer in a molar ratio of 1:1 with 30 wt% TMP and 0.2 wt% AIBN. The mixture was stirred for 1 h at 25 °C and then heated at 60 °C to initiate the polymerization for 4 h then collecting the PTF-PE-SPE. By the same procedure, the PE-SPE was synthesized without adding the TF monomer. The same approach was applied to prepare PE/LiTFSI, PSF-PE/LiTFSI (molar ratio, SF/PE = 1:1), PNF-PE/LiTFSI (molar ratio, NF/PE = 1:1) and PTF-PE/LiTFSI samples without adding TMP. Furthermore, the polymers of PE, PSF-PE, PNF-PE and PTF-PE were synthesized without adding LiTFSI and TMP.

Assembly of coin-type LMBs and pouch cells

Li|LRMO coin cells (2025 type, aluminized steel shell) were assembled in an argon (Ar)-filled glovebox with $H_2O < 0.1$ ppm and $O_2 < 0.1$ ppm. First, the LRMO cathode with 3.5 mg $\mathrm{cm^{-2}}$ (about 1 mAh $\mathrm{cm^{-2}}$) was placed in the cathode case and then 25 µl of the polymerized precursor was added to the surface of the LRMO cathode. Then, a polyethylene separator was placed on the LRMO cathode, and 25 µl of the polymerized precursor was added to the surface of the polyethylene separator in turn. Subsequently, Li metal anode was placed on the surface of polyethylene separator, and the coin cell was sealed. Finally, the coin cell was subsequently polymerized at 60 °C for 4 h. The coin cells were rested at 25 °C for 12 h before testing. Li|$LiNi_{0.8}Co_{0.1}Mn_{0.1}O_2$ (NCM811) coin cells were assembled in the same way. Cu|LRMO pouch cells (85 × 45 $\mathrm{mm^2}$) were assembled in a dry room at a dew point of −60 °C. The 6-µm-thick Cu current collector was used as the anode in the absence of a Li metal foil. The LRMO cathode with high compact density (2.4 g $\mathrm{cm^{-3}}$) and high loading was infiltrated by carbonate electrolyte with 4 µl $\mathrm{cm^{-2}}$ (1.2 M $LiPF_6$ in ethylene carbonate, propylene carbonate and ethyl methyl carbonate (3:2:4 by volume)). The mass loading of anode, cathode, electrolyte and other components is provided in Supplementary Table 1. First, the LRMO cathodes and Cu current collectors were stacked layer by layer with a polyethylene separator to assemble 20 anode|polyethylene|cathode units, followed by packing in an aluminium-plastic film package. Second, to mitigate oxygen-induced radical quenching during in situ polymerization, the prepolymerized SPE precursor was injected into the pouch cell in an Ar-filled glovebox, followed by three cycles of vacuum evacuation (−85 kPa) to rigorously eliminate residual oxygen and moisture. The pouch cell was subsequently hermetically sealed under vacuum to preserve the oxygen-free environment. Finally, after resting for 24 h at 25 °C, the pouch cell was polymerized at 60 °C for 6 h. By the same procedure, Li|LRMO pouch cells (85 × 45 $\mathrm{mm^2}$) were assembled in a dry room at a dew point of −60 °C. The Li anode was rolled 50-µm-thick Li foil Li foils on both sides of Cu foils.

Electrochemical tests

All coin cells were measured on a LAND multichannel battery testing system (Wuhan LAND Electronics) at 25 °C. Li|LRMO cells were cycled in the voltage range of 1.8–4.7 V at 0.05 C/0.1 C for the initial activation cycle and then at 0.5 C/1.0 C for the subsequent cycles (1.0 C = 250 mA $\mathrm{g^{-1}}$). Pouch cells were cycled in the voltage range of 2.0–4.7 V at 0.05 C under 25 °C. The cycling performance of the pouch cells was tested under a fixing device to provide 1.0 MPa external pressure. Electrochemical measurements were carried out on an electrochemical station (Solartron EnergyLab XM). The electrochemical impedance spectroscopy (EIS) during charging of lithium batteries was tested at a frequency range from 1 MHz to 0.1 Hz at an amplitude of 10 mV. The ionic conductivity was tested by EIS. The electrochemical stability window (ESW) of the SPEs was measured at 25 °C by linear sweep voltammetry using a carbon-coated Al|polymer electrolyte|Li metal model at a scan rate of 0.5 mV $\mathrm{s^{-1}}$ from 0 V to 7.0 V. Potentiostatic hold experiments were performed by holding for 3 h at increasingly higher potentials, and the current response was recorded with the same battery model. Electrochemical floating experiments for long times are less susceptible to the influence of impurities.

Calculation of diffusion coefficient

The Li^+ chemical diffusion coefficient ($D_{\mathrm{Li^+}}$) in the cathode is characterized by the GITT, which is performed to confirm the Li^+ insertion–extraction kinetics in the cathode. According to previous studies, the $D_{\mathrm{Li^+}}$ is calculated as

$$D_{\mathrm{Li^+}} = \frac{4}{\pi\tau}\left(\frac{n_{\mathrm{m}}V_{\mathrm{m}}}{S}\right)^2\left(\frac{\Delta E_{\mathrm{s}}}{\Delta E_{\mathrm{t}}}\right)^2 \tag{1}$$

$$\tau \ll \frac{L^2}{D_{\mathrm{Li}}} \tag{2}$$

where τ represents the relaxation time. Here, n_{m} is the mole value, V_{m} represents the mole volume, S represents the contact area of cathode/electrolyte, L represents the diffusion length of lithium ions, ΔE_{s} refers to the voltage response under the pulse current and ΔE_{t} is the voltage change through the galvanostatic discharge.

Materials characterizations

The cycled Li|LRMO cells were disassembled in the Ar-filled glovebox, and the LRMO cathode and Li anode were recollected, followed by washing three times with 1,2-dimethoxyethane solvents to remove the residual electrolyte. The morphology characterization of the electrodes and relevant elemental distribution analysis were conducted using SEM (JSM 7401F at 5.0 kV) and TEM (JEOL at 120 kV). XPS (Kratos Analytical, Axis Supra$^+$) with an Al Kα radiation was conducted to investigate the surface/interface chemistry of electrodes at different voltages. The depth profiles were etched by Ar^+ sputtering at 2 kV. XPS spectra were acquired with a 0.1 eV resolution for C 1*s*, O 1*s*, F 1*s* and Mn 2*p*. The analysis of the Mn 2*p* spin–orbit splitting was not performed, owing to its low signal-to-noise ratio. TOF-SIMS (5–100; IONTOF) was also carried out to investigate the surface/interface chemistry. Raman measurements were performed on a Horiba HR 800 spectrometer equipped with a 785-nm laser as the excitation source. The air-sensitive samples were sealed in a cuvette. Broadband dielectric spectroscopy measurement was conducted on a Novocontrol Concept 80 broadband dielectric spectrometer (Montabaur, Germany) with temperature control. The applied voltage was 1.0 V_{rms} (that is, root-mean-square voltage) with frequency ranging from 10^{-2} Hz to 10^6 Hz at 25 °C. The operando differential electrochemical mass spectrometer (DEMS) experiment was tested using a commercial quadrupole mass spectrometer (Hiden

Analytical) and a home-made Swagelok-type cell. The flow rate was adjusted using a digital mass flow meter (Bronkhorst). The cell construction was accomplished in an Ar glovebox. High-purity Ar at a speed of 1.2 ml min^{-1} was used as the carrier gas on cycling. The DEMS cell was operated using a LAND battery test system. The cell was charged and discharged at 0.1 C. DSC (NETZSCH DSC-200PC Instrument), in situ attenuated total reflection Fourier transforms infrared (ATR-FTIR, NICOLET 6700) and NMR (JNM-ECZ600R) were applied to characterize the structure of the materials. The pulsed field gradient (PFG) NMR technique was applied to investigate the Li$^+$ transference number of polymer electrolytes. ^{7}Li- and ^{19}F-PFG measurements were performed to determine the self-diffusion coefficients of Li$^+$ and TFSI$^-$. Appropriate diffusion delay (Δ) and gradient pulse duration (δ) were selected to ensure a sufficient signal decay. Self-diffusion coefficients were calculated by fitting peak integrals to the Stejskal–Tanner equation. The Li$^+$ transference number was calculated by the following equation:

$$t_{\mathrm{Li}^+} = \frac{C_{\mathrm{Li}^+} \cdot D_{\mathrm{Li}^+}}{C_{\mathrm{Li}^+} \cdot D_{\mathrm{Li}^+} + C_{\mathrm{anion}} \cdot D_{\mathrm{anion}}} \quad (3)$$

where $D_{\mathrm{Li+}}$ and D_{anion} are the measured self-diffusion coefficients for Li$^+$ and anion, and $C_{\mathrm{Li+}}$ and C_{anion} are the concentrations of Li$^+$ and anion, respectively.

Safety performance test

The nail penetration test was carried out in a commercial nail penetration system (BE Nail Penetration Tester, BE-6047C-20T). A 5 mm diameter tungsten steel nail was driven at a speed of 3 cm s^{-1} with a pressure of 13 MPa through the LRMO-based pouch cells with 100% stage of charge (SOC). The thermal test was carried out in an oven by storing at 120 °C for 6 h. The thermal behaviour of the LRMO-based pouch cells with 100% SOC was characterized by an EV-ARC in a standard heat–wait–seek procedure.

DFT calculations

The DFT calculations were carried out in the Gaussian (G16)[35] program with Becke's three-parameter hybrid method using the Lee–Yang–Parr correlation functional (B3LYP)[36] at 6-311 + G(d,p) level. The solvation effect was considered with the universal solvation model of SMD[37] using parameters of PE and PTF-PE, whose dielectric constants were experimentally measured (Supplementary Fig. 11). Frequency analysis was conducted to ensure the ground state of molecular structures. Based on the optimized structures, the HOMO energy level, the LUMO energy level and corresponding atomic orbital components were analysed using the natural bond orbital theory[38].

The binding energy (E_{b}) between a Li$^+$ and a polymer molecule is defined as follows:

$$E_{\mathrm{b}} = E_{\mathrm{Li}^+\text{–polymer}} - (E_{\mathrm{Li}^+} + E_{\mathrm{polymer}}) \quad (4)$$

where $E_{\mathrm{Li}^+\text{–polymer}}$, E_{Li^+} and E_{polymer} represent the energy of the Li$^+$–polymer cluster, Li$^+$ and polymer, respectively.

The oxidation potential (E_{ox}) of PE and PTF-PE polymers was calculated based on the following formula:

$$E_{\mathrm{ox}} = \frac{G_{\mathrm{ox}} - G_{\mathrm{init}} + \Delta G^{\circ}_{\mathrm{solv}}(\mathrm{ox}) - \Delta G^{\circ}_{\mathrm{solv}}(\mathrm{init})}{F} - 1.4 \quad (5)$$

where G_{ox} and G_{init} are the free energies of the oxidized and initial polymer in the gas phase at 298.15 K and 1 atm, respectively. $\Delta G^{\circ}_{\mathrm{solv}}(\mathrm{ox})$ and $\Delta G^{\circ}_{\mathrm{solv}}(\mathrm{init})$ are the corresponding free energies of solvation from gas phase to liquid phase at the standard condition (298.15 K, 1 M). It should be noted that the free energy change corresponding to the state change from 1 atm in the gas phase to 1 M in the liquid phase is 1.89 kcal mol^{-1}. However, as the initial state is subtracted from the oxidized state, the 1.89 kcal mol^{-1} term cancels out and therefore does not appear in the equation. F is the Faraday constant, and the subtraction of 1.4 V accounts for the conversion to the Li/Li$^+$ potential scale. IUPAC (the International Union of Pure and Applied Chemistry) recommends a standard hydrogen electrode value of −4.44 V in the absolute potential scale, leading to the conversion factor of 1.4 V for Li/Li$^+$ potential scale, as Li/Li$^+$ has a value of −3.05 V in the absolute potential scale[39].

Data availability

The data that support the findings of this study are available from the corresponding author upon request. Source data are provided with this paper.

34. Kong, W.-J. et al. Bulk/interfacial structure design of Li-rich Mn-based cathodes for all-solid-state lithium batteries. *J. Am. Chem. Soc.* **146**, 28190–28200 (2024).
35. Frisch, M. J., et al. *Gaussian 16 Rev. C.01* (Gaussian, 2016).
36. Becke, A. D. Density-functional thermochemistry. III. The role of exact exchange. *J. Chem. Phys.* **98**, 5648–5652 (1993).
37. Marenich, A. V., Cramer, C. J. & Truhlar, D. G. Universal solvation model based on solute electron density and on a continuum model of the solvent defined by the bulk dielectric constant and atomic surface tensions. *J. Phys. Chem. B* **113**, 6378–6396 (2009).
38. Reed, A. E. et al. Intermolecular interactions from a natural bond orbital, donor-acceptor viewpoint. *Chem. Rev.* **88**, 899–926 (1988).
39. Trasatti, S. The absolute electrode potential: an explanatory note. *Pure Appl. Chem.* **58**, 955–966 (1986).

Acknowledgements This work was supported by the National Key Research and Development Program (2021YFB2500300), the National Natural Science Foundation of China (22393900, 22393903, 22409114, 21825501 and T2322015), the Beijing Municipal Natural Science Foundation (L247015, L233004 and L243019), the China Postdoctoral Science Foundation (2023M731920), the Discipline Breakthrough Precursor Project of the Ministry of Education of China and the Tsinghua University Initiative Scientific Research Program.

Author contributions X.-Y.H. C.-Z.Z. and Q.Z. proposed the research. X.-Y.H. performed the electrochemical measurements, characterized materials, analysed the data and wrote the paper. W.-J.K. performed the Raman characterization and supervised the analysis of LRMO cathodes. Y.L. helped with the electrochemical experiments. J.-L.L. and L.S. helped with the XPS tests. N.Y. and X.C. performed the theoretical calculations. P.X. helped with the TOF-SIMS tests. Z.-Y.S. and X.-Y.H. assembled the pouch cells. C.-Z.Z., S.S., W.-Z.H., X.C., J.-Q. H., L.A.A. and Q.Z. revised the paper. All authors engaged in the discussion of the results.

Competing interests The authors declare no competing interests.

Additional information

Supplementary information The online version contains supplementary material available at https://doi.org/10.1038/s41586-025-09565-z.

Correspondence and requests for materials should be addressed to Chen-Zi Zhao or Qiang Zhang.

Peer review information *Nature* thanks Xiulin Fan, Jinsoo Kim, Faezeh Makhlooghiazad and Yingjin Wei for their contribution to the peer review of this work.

Reprints and permissions information is available at http://www.nature.com/reprints.